TU Delft

Delft University of Technology

On the importance of the flow field in inexpensive optical aerosol particle counting and sizing

Loizidis, Charis; Skourides, Christoforos; Bezantakos, Spyros; Hadjigeorgiou, Neoclis; Biskos, George

DOI
10.1038/s41598-025-11785-2

Publication date
2025

Document Version
Final published version

Published in
Scientific Reports

Citation (APA)
Loizidis, C., Skourides, C., Bezantakos, S., Hadjigeorgiou, N., & Biskos, G. (2025). On the importance of the flow field in inexpensive optical aerosol particle counting and sizing. *Scientific Reports*, *15*(1), Article 35259. https://doi.org/10.1038/s41598-025-11785-2

Important note
To cite this publication, please use the final published version (if applicable).
Please check the document version above.

Copyright
Other than for strictly personal use, it is not permitted to download, forward or distribute the text or part of it, without the consent of the author(s) and/or copyright holder(s), unless the work is under an open content license such as Creative Commons.

Takedown policy
Please contact us and provide details if you believe this document breaches copyrights.
We will remove access to the work immediately and investigate your claim.

This work is downloaded from Delft University of Technology.
For technical reasons the number of authors shown on this cover page is limited to a maximum of 10.

scientific reports

Check for updates

OPEN

On the importance of the flow field in inexpensive optical aerosol particle counting and sizing

Charis Loizidis[1], Christoforos Skourides[1], Spyros Bezantakos[1], Neoclis Hadjigeorgiou[1] & George Biskos[1,2]✉

Optical Particle Sizers (OPSs) are widely used for measuring size distributions of particles larger than ca. 0.2 μm. To do so, they use mirrors or lenses to gather light scattered by particles passing through a focused beam, directing it to a photo-detector that produces electric pulses from the scattering events. Considering their ability to provide near real-time measurements with minimal attendance and maintenance, and to expand the networks of Particulate Matter (PM) monitoring, several manufacturers have developed low-cost and compact OPS systems. Despite that low-cost OPSs are already available in the market and employed for monitoring PM concentrations, their reported values typically deviate from those of high-end instruments, warranting further efforts to improve their performance. In this work, we designed and built a custom-made yet inexpensive OPS optical system, and studied its performance using a combination of computational and experimental methods at different flow conditions. Our results demonstrate the importance of the flow field within the OPS optical system, and how this can affect its counting and sizing ability. The overall performance of our OPS optical system is very similar to that of high-end instruments, exhibiting a counting efficiency of 50% for particles having a diameter of 320 nm, and a sizing resolution of below 15% for 500-nm particles, complying with the ISO 21501-1 and 21501-4 standards.

Optical Particle Sizers (OPSs) are widely used instruments for measuring the size distributions of gas-suspended particles having diameters in the range from ca. 0.2 to 20 μm[1,2]. The size distributions obtained by OPSs can be used to determine particle mass concentrations expressed as Total Suspended Particulates, or of any class of Particulate Matter (PM) including regulatory values of PM_{10} and $PM_{2.5}$[3]. Apart from being employed as standalone instruments, OPSs can also be used as part of integrated systems for probing intrinsic properties of aerosol particles including their morphology and optical properties[4,5], or the ability to act as cloud condensation nuclei[6–8].

OPSs rely on the capacity of the particles to scatter light, typically from monochromatic laser sources[9], or white-light sources such as Light Emitting Diodes (LEDs)[10]. Part of the scattered light from the particles is gathered by mirrors or lenses on the sensing surface of a photo-detector, producing a signal of discrete pulses[1] that corresponds to single particles passing through the optical detection volume; i.e., the volume created by focusing the light coming from the laser or white-light source.

A number of commercial OPSs are currently available in the market, including model 3330 manufactured by TSI®, models 1.108 and 1.109 by GRIMM®, and model Fidas by PALAS®. The cost of these instruments, however, is in the order of ten thousand euros or more, which prohibits using many of them in dense air quality monitoring networks. As a result, a number of manufacturers have developed low-cost and portable optical particle counters, some also with particle sizing capabilities, over the last decade[11–19], creating new opportunities for distributed field measurements of ambient PM.

The performance of the OPS relies on the quality of the signal reported by its photo-detector, which primarily depends on the alignment of all the parts of the optical system of the instrument, as well as the quality of its electronic components. More specifically, the detection efficiency and resolving power of the OPS is determined by the optical detection volume that is defined by i. the focusing of the light source at the centerline of the sampled aerosol flow, ii. the probability of the sampled particles to pass through the more focused areas of the light beam (the higher this probability, the stronger the resulting pulses from the scattering events as explained below), and iii. the effective reflection of the scattered light to the sensing surface of the photo-detector. Adjusting

[1]Climate and Atmosphere Research Center, The Cyprus Institute, 2121 Nicosia, Cyprus. [2]Faculty of Civil Engineering and Geosciences, Delft University of Technology, Delft 2628CN, The Netherlands. ✉email: g.biskos@cyi.ac.cy; g.biskos@tudelft.nl

all these parameters independently to produce expected signal ranges by the scattering particles is a challenging task, which is the reason that OPSs require calibration with reference particles after they are assembled.

In this work, we designed and built a custom-made and cost-effective OPS optical system (OPS-OS), and studied its performance under different sample flow fields. The OPS-OS is designed in a way that assembly and alignment of all system components can be done in an easy and effective way. Its electronics circuit was designed to provide signals with a low noise, having the ability to produce discrete pulses that can effectively be inverted to particle size distributions. For the needs of the study, the OPS-OS was built in a versatile manner to allow manipulation of the flow field and explore how the aerosol and sheath flow-rates, as well as the diameter of the aerosol inlet/outlet tubes and their distance from the focused light beam, can affect the performance of the system.

We used COMSOL to determine parameters that affect more strongly the focusing of the particles through the optical detection volume, and consequently the performance of the OPS-OS in terms of sizing resolution. Leveraging the flexibility offered by 3D printing, we modified different parts of the OPS-OS chamber in order to experimentally confirm the COMSOL results and identify the optimum set of design and operating parameters. Finally, using a set of well-functioning flow conditions, as those were identified by the simulations and the experiments, we determined the particle counting and sizing performance of the custom-made OPS-OS following the standards defined by ISO 21501-1[20] and 21501-4[21] protocols, and compared it with that of a high-end instrument (i.e., a TSI, model 3330).

The rest of the paper is structured as follows: the "Operating principle" section provides a brief description of the operating principle of the OPS, with some theoretical background given in the Supplementary Information (SI), the "Experimental setup and procedures" section describes the experimental setup and methods we employed, whereas the "Results and discussion" and "Conclusions" sections, respectively, discuss our results and highlight the most important conclusions.

Operating principle

When light interacts with a particle suspended in a gas medium, part of it is absorbed and another part is scattered[22]. The amount of light scattered or absorbed depends on the size, the morphology and the composition of the particles, which together define their optical behaviour. For very small particles (i.e., particles smaller than ca. 5% of the light wavelength), the light scattering is governed by Rayleigh's theory[23,24]. When the size of the particles becomes comparable to the wavelength of the incident light (ranging from ca. 400 to 1300 nm for laser diodes typically employed in OPS-OSs), Mie's scattering theory (see Section S1 in the SI), which is a rigorous solution of Maxwell's equations describing the interaction of electromagnetic waves with spherical particles, is more appropriate to use.

The electrical signal V_{sig} produced by the photo-detector of OPS-OSs when receiving light scatted by the sampled particles depends on a number of parameters, including the wavelength λ and the illuminating intensity of the light source, the range of scattering angles θ used to record the scattering events, the specifications of the photo-detector, as well as the diameter d, morphology, and refractive index m of the particles. In practice, the photo-detector signal can be approximated by:

$$V_{sig} = A \cdot Q_{sca}\left(\lambda, \theta, d, m\right), \tag{1}$$

where A is an instrument-specific factor (see Eq. S20 in the SI for details), and Q_{sca} the particle-size-dependent scattering coefficient that can be determined by Mie's theory, which is calculated here using the code developed by Rosenberg et al.[25] (see Section S1 in the SI for more details). The wavelength and the range of scattering angles contributing to the signal of an OPS-OS are design-specific parameters, both of which are specified in order to maximise the signal from the single-particle events (see Section S1 and Fig. S1 in the SI). Considering those values as given, one needs to assume the shape and refractive index of the particles in order to determine their size (specifically their optical equivalent diameter d_{oe}) from the signals recorded by the photo-detector and Eq. 1. To this end, Polystyrene-Latex (PSL) particles, which have a spherical shape and a refractive index of $1.59 + 0i$, are typically used to calibrate OPSs and consequently provide the assumed parameters for determining d_{oe} in subsequent measurements.

Operating conditions that can yield good sizing resolution require that only one particle passes through the optical detection volume in the OPS-OS each time, producing a single pulse on the photo-detector. Considering that, the concentration of the sampled particles can be determined as[26,27]:

$$C = \frac{N}{Q \cdot \Delta t}, \tag{2}$$

where N is the number of pulses (also referred as events) produced during the time interval Δt, and Q is the volumetric flow rate of the aerosol that passes through the OPS-OS. Typically, OPSs use a sheath flow to dilute the sampled aerosol and to confine the particles within a narrow beam before those are passed through the optical detection volume. The total sample flow through the OPS-OS, Q, is therefore the sum of the aerosol and sheath flows (i.e., $Q = Q_a + Q_s$), which are independently controlled. Use of the sheath flow yields a dilution factor of $L = 1 + Q_s/Q_a$, that needs to be taken into account when determining the particle number concentration by Eq. 2 (i.e., $C_c = L \cdot C$).

The sizes of the particles sampled by OPSs are determined from the height of the pulses produced by the photo-detector when receiving the light they scatter as they pass through the focused light beam (i.e., the optical detection volume). We should note here that the raw signal from the photo-detector of OPS-OSs contains a certain amount of noise, defined also by the quality of the required electronic components (see Section S3 in

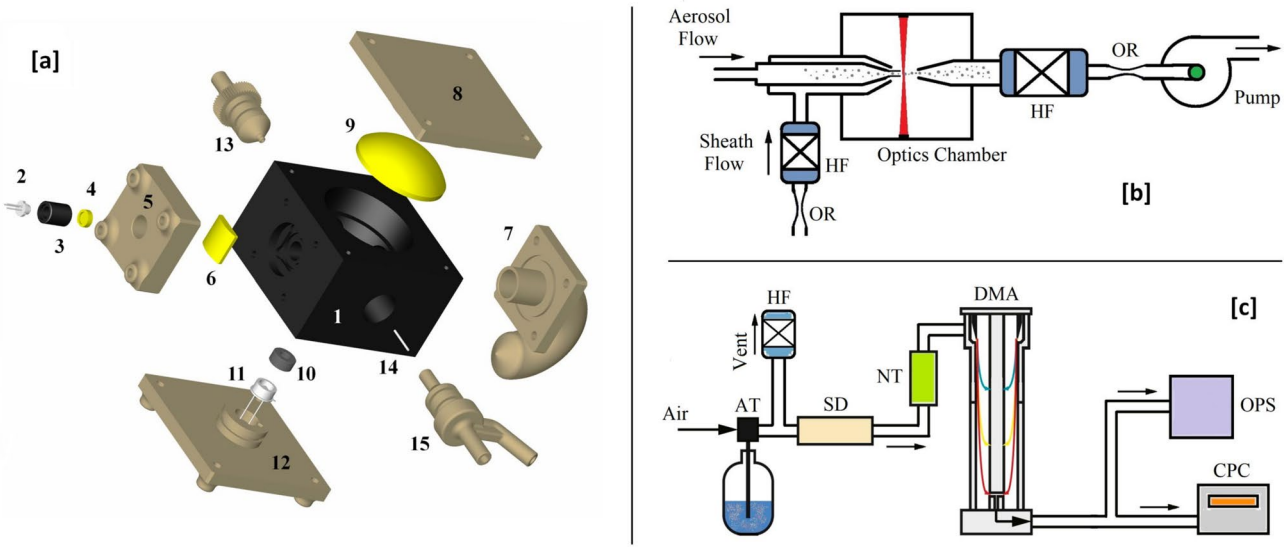

Fig. 1. Schematic diagrams showing (**a**) a blown-up drawing of the OPS-OS with all its parts (see Table 1 for more details), (**b**) the flow diagram of the OPS, and (**c**) the setup used for our experiments. Key: OR, orifice; AT, atomiser; HF, HEPA filter; SD, silicon dryer; NT, charge neutralizer; DMA, differential mobility analyzer; OPS, optical particle sizer; CPC, condensation particle counter. Images were created in SolidWorks, version 2020 (**a**) and in Adobe Illustrator version CS6 (**b** and **c**).

	Name	Utility
1	Optics shell	Holding and aligning all the components together
2	Laser diode	Light source of specific wavelength
3	Laser holder	Aligning the laser diode with the collimating lens
4	Collimating lens	Making a parallel laser beam
5	Laser socket	Holding and aligning the laser parts
6	Cylindrical lens	Focusing the laser beam
7	Beam dump	Absorbing the laser light
8	Mirror socket	Holding and aligning the mirror
9	Spherical mirror	Focusing the scattered light to the photo-detector
10	Detector cover	Covering the photo-detector non active surface
11	Photo-detector	Converting scattered light to electrical signal
12	Detector socket	Holding and aligning the photo-detector
13	Flow outlet	Exhaust aerosol flow
14	Dispensing tip	Adjusting the aerosol tube diameter
15	Flow inlet	Aerosol and sheath flow entrance

Table 1. List of the OPS-OS components.

the SI), and thus only pulses above this level are considered as particle events in the data analysis. Calibration of the particle sizes reported by OPSs is carried out by feeding them with monodisperse PSL particles of different known sizes, and recording the pulse heights. Due to beam intensity non-uniformities within the optical detection volume, however, this yields pulses that have a range of heights, distributed around a mean value (see Sect. 3 for more details), for each size of PSL particles. All the mean pulse heights corresponding to PSL particles of different size are then used to fit Eq. 1, and thus to derive the instrument-specific factor A. Once this is achieved, the number and the width of the size bins is defined before converting the raw measurements to particle size distributions.

Experimental setup and procedures

Details of the OPS-OS we designed and built, and of the experimental setup we employed to test it are provided in Fig. 1. More specifically, Fig. 1a shows a blown-up drawing of the OPS-OS including all its parts as those are described in Table 1, whereas Fig. 1b provides a schematic illustration that reflects its operating principle. Parts 1 and 3 were manufactured by anodized aluminum using Computer Numerical Control (CNC) machining[28], whereas parts 5, 7, 8, 10, 12, 13 and 15 were 3D-printed by Stereolithography (SLA)[29] using a black resin (FEP-

shop Resin, Tough). SLA is highly flexible[30], and the 3D-printer we employed (Phrozen, Model Mini-4k) provides the ability to manufacture complex curved-hollow yet highly robust and airtight parts such as the beam dump and the flow inlet (i.e., parts 7 and 15) in our OPS-OS. Parts 2, 3, 4, 6, 9, 11 and 14 were purchased from different manufacturers (their specifications are provided in Table S1 in the SI).

Parts 1 and 3 were manufactured by CNC machining because they define the most critical distances between the optic parts, which require low tolerances and materials that do not easily deform. Other important components are parts 13 (3D-printed flow outlet), 14 (dispensing tips available in the market), and 15 (3D-printed flow inlet) that define the flow field within the OPS-OS, with parts 14 and 15 forming the sample flow inlet. Sections S2 and S3 in the SI describe in more detail the basic design features of our OPS-OS and its electronic circuit. The cost of all these components is in the order of €350, which accounts for 70% of the cost for the entire system (i.e., excluding labor, transportation and other costs), making it rather inexpensive (see Section S4 in the SI).

The aerosol and the sheath flows (Q_a and Q_s, respectively) passed through the OPS-OS were regulated by 3D-printed orifices, and monitored with a precision of ± 0.01 L/min by a mass flow meter (TSI, Series 4000) during the experiments. All the measurements were carried out using PSL or ammonium sulfate particles produced by an atomizer (AT; PALAS, AGK-2000) coupled to a silica-dryer (SD) as shown in Fig. 1c. Subsequently all the particles were passed through an aerosol charge neutralizer (NT; TSI, model 3077A) and a differential mobility analyzer (DMA; TSI, model 3081). The monodisperse flow downstream the DMA was split and directed to a condensation particle counter (CPC; TSI, model 3025A) and to the tested OPS-OS. The temperature throughout all our measurements was maintained at ~ 25 °C. To determine the counting efficiency of the OPS-OS for particles larger than ca. 5 μm, we nebulized a salt solution using a Collison Nebulizer (CH-Technologies). This produced polydisperse particles, which were subsequently fed in parallel to the OPS-OS the TSI-3330 OPS (setup not shown here).

A number of combinations of flow parameters were tested in this work (see Table S2 in the SI). For all these tests, we used aqueous solutions of 500-nm PSL spheres (MAGSPHERE, PS500NM), that were further diluted with purified water and atomized using the AT. The resulting aerosol was dried by passing it through the SD, and the dried 500-nm PSL spheres were size-selected by the DMA in order to filter out other particles produced by the atomizer due to impurities in the solvent. We should note here that the PSL particles used in all our tests are not perfectly monodisperse, but their sizes have a very narrow distribution as determined by the manufacturers[31].

The OPS-OS needs ca. 10 min to warm up all its electronic components (in particular the laser diode) before it can carry out stable measurements. The photo-detector provides an analogue output signal, and thus a continuous pulse from single-particle events, that is recorded with a digital oscilloscope (Digilent®, Analog Discovery 2) using the open-source 'WaveForms' software. The photo-detector signal is sampled with a frequency of 2 MHz, yielding at least 11 data points for each pulse considering that those have a duration of ca. 5.5 μs. To collect enough pulses in order to determine the size distribution of the sampled particles, the measurement time was chosen to be ~ 33 s.

Figure 2a provides an example of the OPS-OS raw signal recorded over a period of 1 s during these tests, with the dashed line indicating the noise threshold, V_{trig}, that is set to 30 mV. Figure 2b shows an example of a characteristic pulse taken from this recording. A peak identification algorithm (Peak Detector VI, available in LabView) is used to calculate: i. the total number of pulses in each sample (i.e., N in Eq. 2), ii. their peak height, y, and iii. its second derivative, y'', with respect to time in order to determine the pulse width.

For a number of pulse heights determined over a specific time interval, we then determine the Probability Density Function (PDF) as shown in Fig. 2c. The PDF of the pulse heights (sampled over a period Δt) that are above the noise level (indicated by the values on the right-hand side of the dashed line in Fig. 2c that corresponds to V_{trig}), can be fitted by a log-normal distribution expressed as:

$$h\left(y\right) = \alpha \cdot e^{-\left(\frac{\log(y)-\mu}{\sigma\sqrt{2}}\right)^2}, \tag{3}$$

where α is the amplitude, μ is the mean value, and σ the standard deviation. The fitted values (μ and σ) of Eq. 3 are used to quantify the sizing resolution of the OPS-OS determined from the raw measurements (i.e., pulse height statistics), which can be calculated as:

$$R = \frac{\mu}{2.355 \cdot \sigma}. \tag{4}$$

Considering that the Full Width at the Half Maximum of the PDF ($FWHM_{PDF}$) is $2.355 \cdot \sigma$ (see Ref. [32]), the resolving power can also be expressed as $R = \frac{\mu}{FWHM_{PDF}}$. We should note here that some measurements yield pulse height PDFs that do not exhibit a peak. In these cases, the OPS measurements cannot be used to perform particle sizing at all, and as R is not possible to determine, it is set to zero. In some other cases, the pulse height PDF exhibits a peak that is not well distinguishable from the OPS-OS signal noise[33]. In these cases, the OPS-OS sizing capability is very low (yet difficult to be quantified), and R is set to 1 for the communication of our results in the next section.

The Full Width at Half Maximum of each pulse ($FWHM_p$; see blue line in Fig. 2b), which determines the degree to which individual pulses can be discretized (i.e., low $FWHM_p$ leads to more discrete pulses, especially in higher particle concentrations), can be estimated as[34]:

$$FWHM_p = 2 \cdot \sqrt{-y/y''}, \tag{5}$$

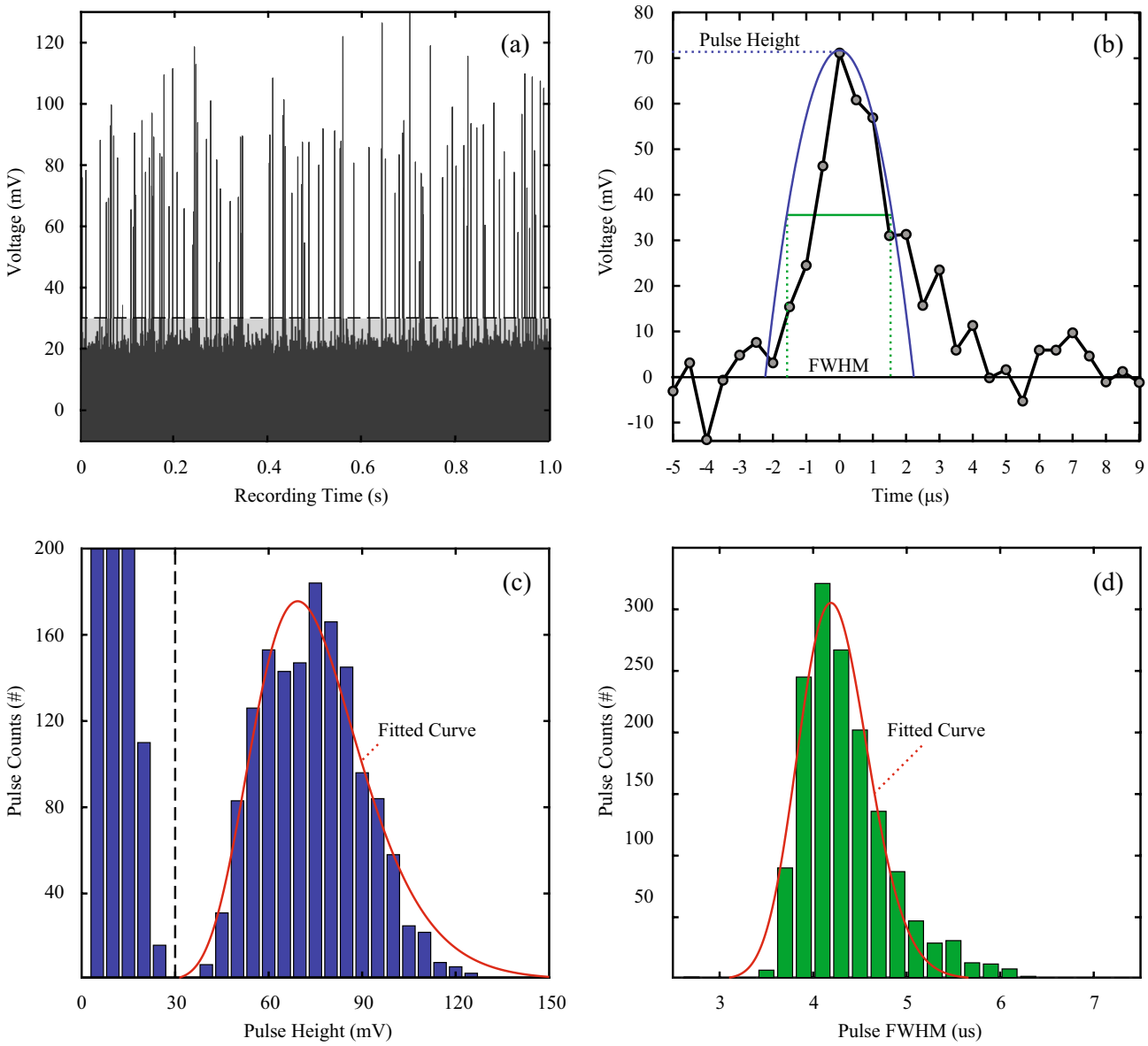

Fig. 2. Example of raw data recorded by the OPS-OS when sampling 500-nm PSL particles, and how those are analyzed: (**a**) pulses recorded by the photo-detector over a sampling period of 1 s, (**b**) recorded signal from the photodetector over a period of 14 µs during which a single pulse of specific height and FWHM is induced by a particle passing through the focused light beam, (**c**) probability density function of all the pulse heights, and (**d**) of their FWHM recorded over a 1-s sampling time. The black dashed lines in subplots (**a**) and (**c**) provide the threshold of the noise level. A quadratic function is fitted to the data points for each pulse, as illustrated in subplot b, in order to obtain its height and FWHM.

To determine $FWHM_p$, y is approximated by a quadratic function that is fitted to the data points of each pulse by the peak finding algorithm, and y'' is determined as the second derivative of that function. An example PDF of the $FWHM_p$ values from the recorded raw measurements (shown in Fig. 2a), is provided in Fig. 2d. Very wide peaks (i.e., with $FWHM_p > 7$ µs) can result from poor focusing of the particle beam and/or of the optical detection volume, or by particle coincidence; i.e., more than one particles passing through the focused part of the light beam at the same time.

Results and discussion

Analysis of the OPS-OS flow field

The flow-field in the OPS-OS geometry was determined using Reynolds-averaged Navier–Stokes (RANS) 'k-ω' turbulent flow model[35] in COMSOL (see Section S5 of the SI for more details). The part of the flow field that defines the performance of the OPS is that between the aerosol inlet tube and the focused light beam. An example solution of the flow field in the OPS-OS is provided in Fig. 3. More specifically, Fig. 3a shows an axisymmetric solution of the velocity profile within the OPS-OS, with the y- and x-axis indicating respectively

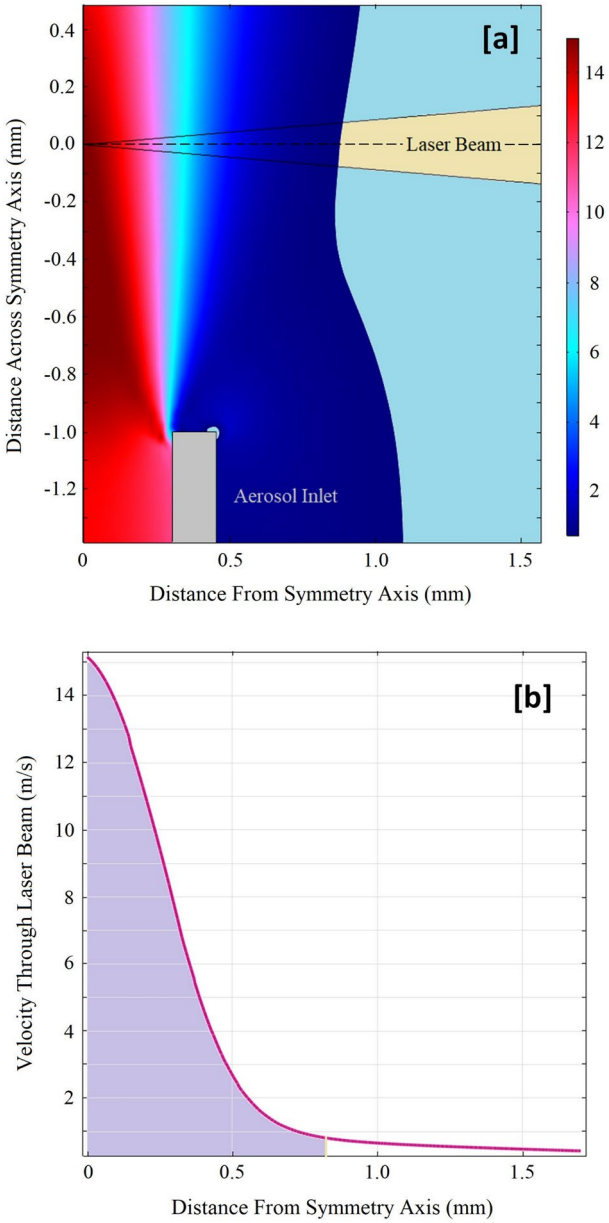

Fig. 3. Results from an example COMSOL simulation showing (**a**) the axisymmetric flow profile within the OPS-OS with the colorbar indicating the magnitude of the velocity in m/s, and (**b**) the velocity distribution at the point where the flow crosses the light beam. The flow input parameter for these example simulations are provided in Table S2 (see gray-shaded cells therein).

the axis of symmetry of the simulated geometry and the radial distance from it. The colorbar shows the velocity of the flow in m/s, whereas the two black solid lines indicate the domain of the focused part of the laser beam.

Figure 3b shows the velocity profile at the level of the laser beam (i.e., along the dashed black line indicated in Fig. 3a). The sampled aerosol forms a jet-like flow[36], the width of which affects the OPS-OS counting and sizing performance. The main challenge therefore, is to ensure that the aerosol jet is as narrow as possible so that the vast majority of the particles pass through the most focused areas of the laser beam where they can scatter light that produces higher and narrower pulses on the photo-detector (due to the higher intensity of the focused laser light and the shorter path of the particles in that). By doing so one can acheive high counting and sizing efficiencies, while avoiding any turbulence in the flow field inside the OPS-OS.

Figure 4 illustrates examples of three possible paths the particles can follow through the OPS-OS. Particles passing through the light-grey shaded area (i.e., trajectory 1) go through the region where the light is highly focused and consequently the induced pulses are more intense. In addition, particles of the same size passing through this region produce reproducible pulses in terms of height because the light is more focused, thereby improving the sizing resolution of the system. Wider aerosol jets will result in particles passing through areas where the light beam is less focused (see trajectory 2 in Fig. 4). In this case, the particles will be detected, but

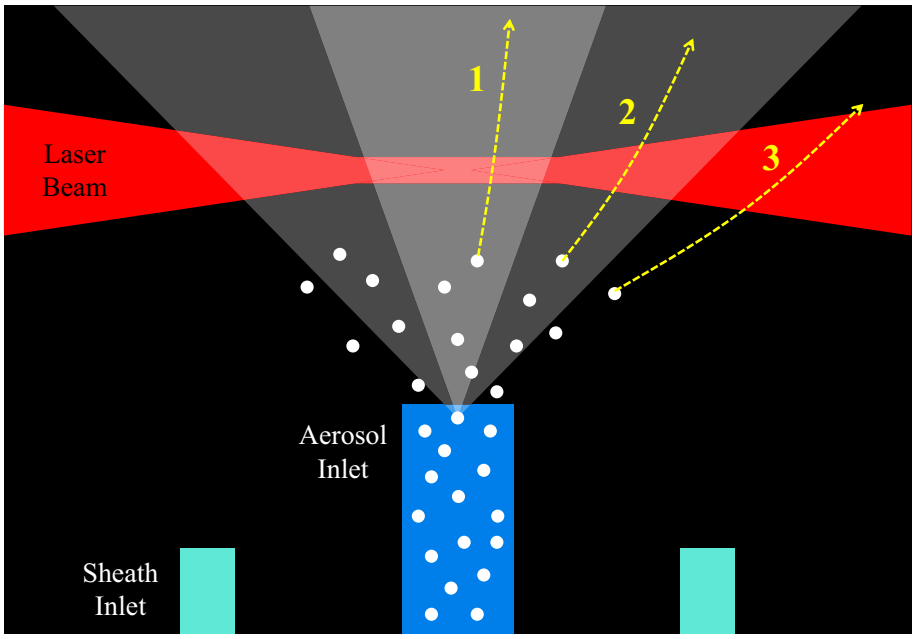

Fig. 4. Illustration showing the possible paths that the sampled particles can follow through the OPS-OS. The light-grey shaded path corresponds to particles that will pass through the more focused region of the light beam, producing high intensity scattering events that will be reflected by the mirror and captured by the photo-detector as high and narrow pulses. The dark-grey region corresponds to particles that will pass through the less-focused regions of the light beam, so the light they will scatter will be reflected by the mirror and captured by the photo-detector as short and wide pulses. Last, particles following trajectories that go through the black region when crossing the light beam will scatter light, but that will not be effectively reflected to the photo-detector.

they will produce wider and less repeatable pulses, thereby reducing the sizing resolution. Even wider aerosol jets and/or intense turbulences will make particles go through areas where the light beam is not focused at all (see trajectory 3 in Fig. 4). In those cases, the particles will not even be counted because the scattered light reflected by the mirror will miss the photo-detector. Considering the geometry of our system and the shape of the mirror we employed, the particles need to be within a distance of ca. 2.5 mm from the flow centerline in order for the scattered light they will produce to be reflected by the mirror to the photo-detector. This is larger than the radius of the wider tubes we employed in the aerosol inlet, ensuring that all the particles will pass through the light beam and be detected for most of the operating conditions we employed. Any particles passing through the light beam at a distance from the centerline that is larger than ca. 2.5 mm, are not counted by the OPS-OS.

The sizing resolution of the OPS-OS can be affected by the aerosol inlet diameter, the distance between the inlet and the laser beam, the total flow rate, and the dilution factor as shown in Fig. 5. The experimental results shown here are qualitatively correlated with and explained by the COMSOL calculations of the flow velocity through the detection volume and/or the aerosol jet diameter. The results are based on the analysis of the data provided in Figs. S9, S10, S12 and S13 in the SI that provide the respective normalized pulse-height PDFs, the $FWHM_p$ PDFs, and the flow field determined by the simulations. Table S2 in the SI shows in detail all the flow-field experimental conditions tested in this work, together with the respective Reynolds (*Re*) numbers of the aerosol at the inlet of the OPS-OS. We should highlight here that the *Re* number of both the aerosol and the sheath flows are always well below 2000, and thus any turbulence predicted in the simulations is attributed to the shear mixing interactions of the two streams (see all the simulations provided in Section S6 of the SI).

The first observation is that a narrow aerosol inlet tube leads to a narrower aerosol jet, which in turn enhances the OPS-OS sizing resolution (as determined through the measurements and Eq. 4). One would expect that the narrower the aerosol tube becomes, the narrower the aerosol jet will be, and thus the size-resolving power of the instrument will increase. However, there is a velocity limit above which the OPS-OS sizing resolution falls abruptly due to internal flow turbulence, as indicated by the simulations (see example in Fig. S13 of the SI), for aerosol inlet tube diameters smaller than ca. 0.3 mm (grey-shaded area in Fig. 5a). Considering that, an optimized aerosol inlet tube is the one having a diameter of 0.6 mm.

As the distance between the aerosol inlet tube and the optical detection volume increases from 1.0 to 7.0 mm, the aerosol jet diameter also increases (as shown in Fig. 5b) and thus the fraction of particles passing through less focused regions of the light beam increases. This yields pulses that are wider and have random heights, and consequently to wider PDFs and thus lower sizing resolution. We should note here that neither the outlet tube diameter nor its distance from the laser beam affect significantly the OPS-OS sizing resolution (see Fig. S11 in the SI), as corroborated also by the COMSOL simulations.

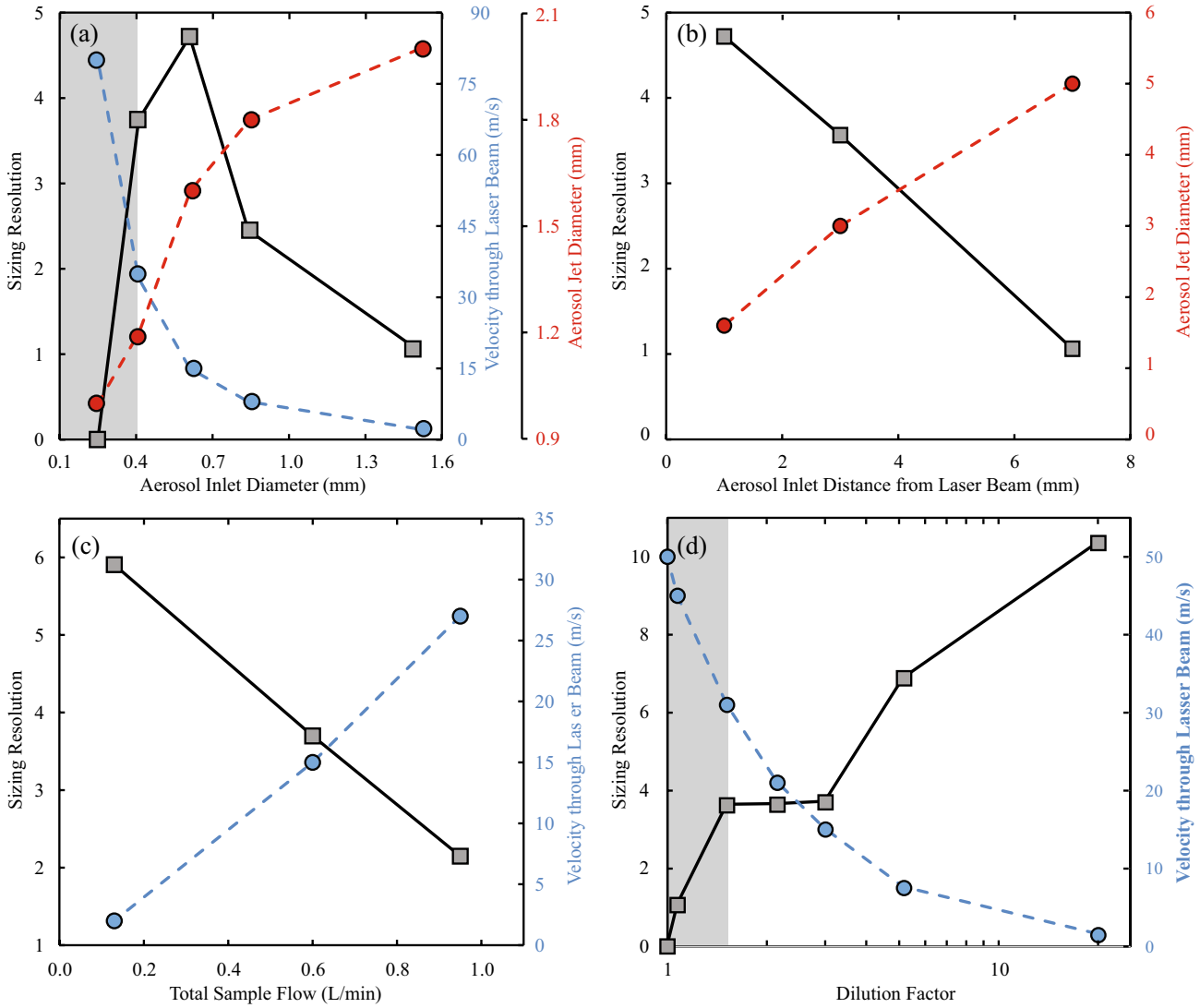

Fig. 5. Correlation between experimentally determined OPS-OS sizing resolution and simulated aerosol jet velocity or diameter as a function of (**a**) aerosol inlet tube diameter, (**b**) the distance between the aerosol inlet tube and the laser beam, (**c**) the total flowrate through the system, and (**d**) the dilution factor.

Apart from the geometrical characteristics of the OPS-OS flow nozzles, the flow rates passed through the OPS-OS are also very important. To investigate the effect of the total sample flow to the performance of the instrument, we varied that from 0.15 to 1.00 L/min while keeping the dilution factor L fixed to ca. 3 ± 0.27 L/min. As indicated by the COSMOL simulations (see Fig. S12 in the SI) the flow field remained laminar for all these conditions, but as shown in Fig. 5c, the size-resolving power of the OPS-OS decreased with the total flow, but not at a level that becomes very low (i.e., ≤ 1). The decreased sizing resolution at the highest total flow we tested can be explained by the photo-detector response time (ca. 2 μs rising time; see section S3 in the SI): i.e., at very high crossing velocities through the laser beam, the photo-detector does not have enough time to reach the peak pulse height because the residence time of the particle in the laser beam is very small.

Figure 5d shows the sizing resolution of our system and the velocity through the optical detection volume as a function of the dilution factor L. As expected, the sizing resolution increases with increasing the dilution factor (by increasing the sheath-to-aerosol flow ratio). In the cases where the sheath flow is significantly higher than the aerosol flow (i.e., for $L > 3$), the sheath flow velocity becomes comparable with the aerosol velocity through the laser beam resulting in narrower aerosol flow jet (see Fig. S13a and b), which in turn appears to confine the particle trajectories, making them to pass through the most focused areas of the laser beam (see trajectory 1 in Fig. 4). On the other hand, for L values smaller than ca. 1.7 (marked with grey region in Fig. 5d) we observe turbulence in the simulations (see Figs. S13 and S14 in the SI), similarly to the cases of very small aerosol inlet diameters (see Fig. 5a), that takes the particles away from the paths that go through the focused region of the light beam, leading to an abrupt decrease in the sizing resolution.

Generally, the highest OPS-OS sizing resolution values were achieved at relatively lower Re numbers (< 400) in the aerosol inlet tube (see Fig. S16 in the SI). This wre achieved by either increasing the diameter of the inlet

tube or decreasing the flow rate. Considering, however, that the aerosol inlet tube has to be narrow enough to produce an aerosol jet flow that will go through the more focused region of the light beam in order to produce a signal on the photo-detector (i.e., a region that is a couple of millimeters wide), the only way to restrict turbulence in the aerosol inlet tube is to keep the aerosol flow rate at a minimum value. This in turn confines the sheath flow rate considering that in the ideal situation the velocities of the two streams (aerosol and sheath flow) at the point where they meet have to be comparable.

Finally, there is a strong correlation of the $FWHM_p$ of the pulses with the velocity through the laser beam (see Fig. S17 in the SI). This happens because by increasing their velocity the particles spend less time in the beam, thus producing narrower pulses. The $FWHM_p$ PDF is not directly linked to the resolving power of the OPS-OS, but it can provide very useful information on the flow field through and the resolution of the OPS-OS. For example, in the experiments where the aerosol jet diameter is wide (see results in Figs. S9, S10, S12 and S13 of the the SI), we observe a significant number of wider pulses, indicating that many particles do not pass through the focused region of the laser beam (see trajectory 2 in Fig. 4). Similarly, wider pulses are recorded in the cases where turbulence occurs. Generally, the $FWHM_p$ has to be as small as possible in order ensure 100% counting efficiency while avoiding overlap of pulses produced by different particles and thus avoid coincidence error.

Overall performance

Using now a set of well-functioning geometric and operating flow-field parameters (i.e., $Q_s = 0.4$ L/min, $Q_a = 0.19$ L/min, $L = 3$, $D_{aer} = 0.61$ mm, $X_{in} = 1$ mm, $D_{out} = 1$ mm and $X_{out} = 2$ mm; grey-shaded cells in Table S2 of the SI), we calibrated our OPS-OS with particles of different sizes. The signal noise threshold defines the minimum particle size that the OPS-OS can detect (i.e., 30 mV, corresponding to the height of pulses induced by ca. 0.3-μm particles in our case). Figure 6a shows the height of the pulses produced by the OPS-OS when sampling PSL spheres having sizes that range from ca. 0.3 to 5.0 μm. Predictions by Mie's theory (red line in Fig. 6a) are made by fitting Eq. 1 to the measurements. The vertical lines in Fig. 6a indicate the boundaries of the size bins, defined by separating the logarithmic particle size scale in eight equal channels per decade. The pulse-height values where the vertical lines intersect with the theoretical curve in Fig. 6a are the pulse height thresholds of the size bins. Figure 6b provides a comparison between the measured and the nominal size of the test particles, showing an agreement within ± 10%that complies with the ISO 21501-4 requirements (see details of the calculations in Table S4 of the SI).

Figure 6c shows the counting efficiency of the OPS-OS as a function of particle diameter. As described in Sect. 3, to produce particles smaller than ca. 1 μm we atomized an ammonium sulfate solution, and the resulting particles were dried and size/mobility selected by a DMA. To produce larger particles, we nebulized a salt solution using a Collison Nebulizer. In either case, the counting efficiency of the OPS-OS was determined by dividing its counts for specific size bins by the respective counts reported by the TSI-3330 OPS, which was used in all these measurements as a reference instrument[37]. We should note here that the size bins of the OPS-OS were selected to be the same with those used by the TSI-3330 OPS so that the counting efficiency for each size could be determined. Both instruments had their inlet placed vertically, in order to minimize losses of the larger particle[38].

Evidently, our OPS-OS exhibits 50% counting efficiency for particles having diameters of ca. 320 nm, it increases to 100 ± 10% for particles up to ca. 5 μm in diameter in compliance with the revised ISO 21501-1 standard (to be published soon), and drops back to 50% for 9-μm particles. To determine the concentration of particles above which coincidence errors kick in, Fig. 6d shows the counting efficiency as a function of the particle concentration when sampling 500-nm ammonium sulfate particles. For these particles, the counting efficiency remains 100% for relatively high particle concentrations (i.e., ~ 4000 #/cc), dropping to ca. 60% at ~ 7000 #/cc due to particle coincidence.

According to the ISO 21501-4 standards (see Table S3 in the SI), the minimum detectable particle size is the one exhibiting pulse height histograms that have a clear peak; i.e., at least 2 times higher than the noise valley[33]. For our OPS-OS, this minimum size corresponds to ca. 300 nm. It is also evident that the counting efficiency for particle having sizes between 450–600 nm (i.e., 500 nm), which corresponds to 1.5–2 times larger than the smallest particles that can be detected by the OPS, is around 100%, complying with the ISO 21501-1 and 21501-4 requirements. Finally, the particle sizing resolution, determined according to ISO 21501-4 as the standard deviation from the median particle optical equivalent diameters measured from the size distributions (see Eqs. S21-S23 and calculations provided in Table S4 of the SI), is always below 15% (for particle having sizes 1.5–2 times larger than the detection limit); again compatible to ISO 21501-1 and 21501-4 standards. Figures S19 and S20 of the SI provide respectively pulse height PDFs and size distributions determined by the OPS-OS when sampling different particle sizes.

Figure 7 compares the sizing resolution of our custom-made OPS-OS with that of the TSI-3330 OPS when sampling 500-nm PSL particles. Both OPSs exhibit ca. 100% counting efficiency for particles of this size. The blue dashed line corresponds to the sizing standard deviation upper limit of an OPS according to the ISO 21501-4 standards, which is 15% of the median particle size, and the red dotted line to the standard deviation of the DMA transfer function (grey region) when sizing 500-nm particles. Evidently, the OPS-OS developed here exhibits a 10.4% sizing standard deviation, whereas the respective value for the TSI-3330 OS is 7.9%, indicating that both instruments meet the ISO 21501-4 standards.

Conclusions

We have developed a custom-made OPS-OS and studied its performance in terms of sizing resolution by changing its internal flow field. The aerosol inlet tube diameter should be small enough to ensure the formation of a narrow aerosol sample jet but large enough to avoid turbulence (i.e., optimum value estimated to be 0.6 mm for our system). At the same time its distance from the laser beam should be as small as practically possible so

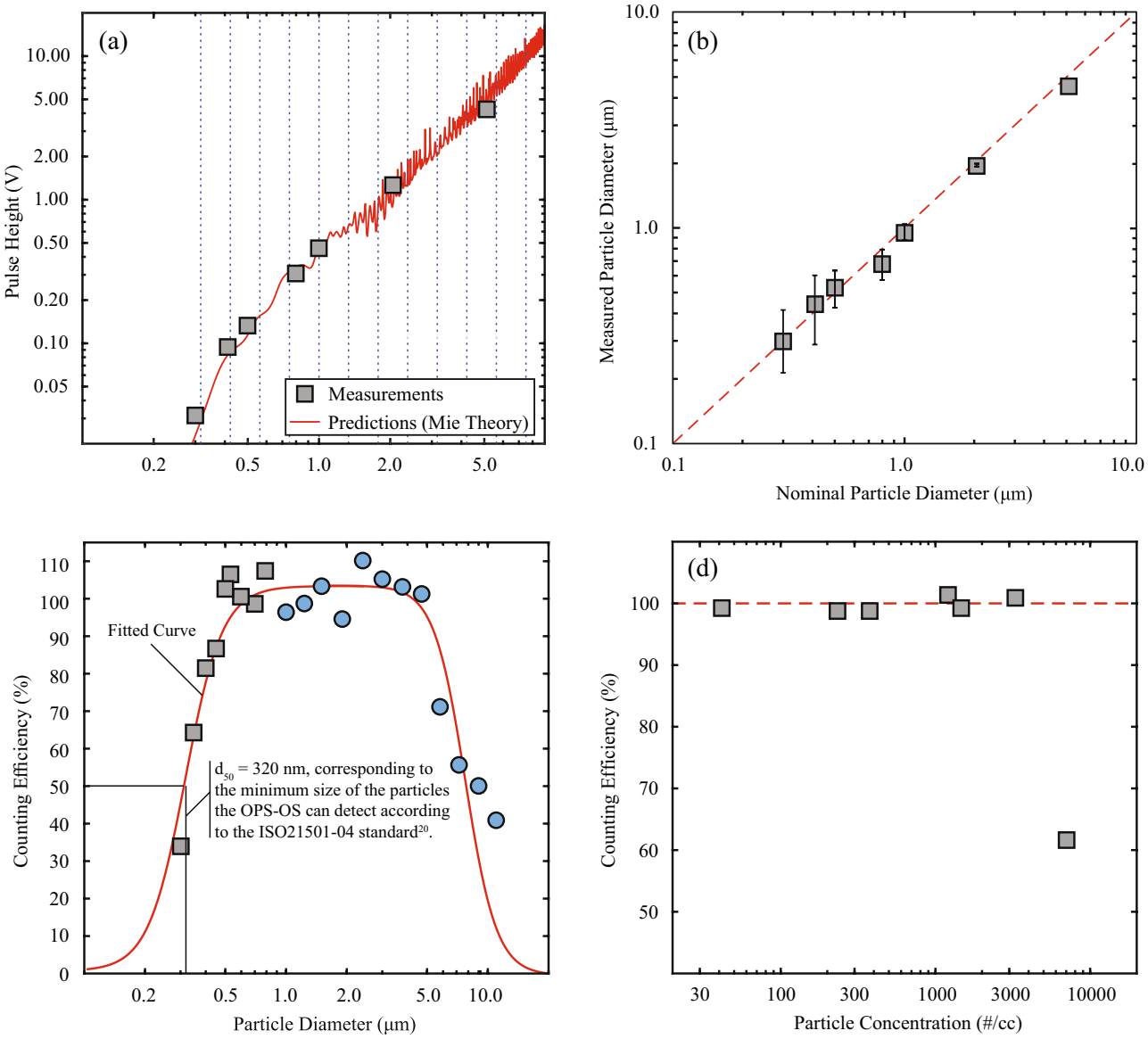

Fig. 6. Calibration and performance evaluation of the custom-made OPS-OS, including (**a**) fitting the Mie theory predictions to the measured pulse height produced by monodisperse particles of different size, (**b**) comparison between measured and nominal size of monodisperse particles, (**c**) counting efficiency as a function of size of the monodisperse (grey squares) and polydisperse (blue circles) particles, and (**d**) counting efficiency as a function of particle concentration for monodisperse PSL spheres having sizes 500 nm. The operating parameters are those provided in the grey shaded cells in Table S2 of the SI.

that the aerosol jet flow does not get too wide causing a big fraction of the sampled particles to pass through the less focused area of the light beam. The speed of the particles passing through the laser beam should be long enough to ensure that the scattering event is captured by the photodetector, which for our case has a response time of ca. 2 µs. This dictates the maximum aerosol flow rate that can be used, provided that turbulence does not occur in the aerosol inlet tube, and in turn the sheath flowrate, which depending on the inlet geometry has to enter the OPS-OS chamber at a similar speed with that of the aerosol flow, and the dilution factor. Our results also show that the performance of the custom-made OPS-OS meets the requirements of ISO 21501-1 and 21501-4, providing measurements that are comparable with a high-end instrument (i.e., exhibiting a sizing standard deviation that is 2.5% higher than that of the TSI-3330 OPS). Considering the lower cost of this system, the work provided here paves the way towards inexpensive counting and sizing of aerosol particles that is very much needed for better understanding their impacts on human health and climate.

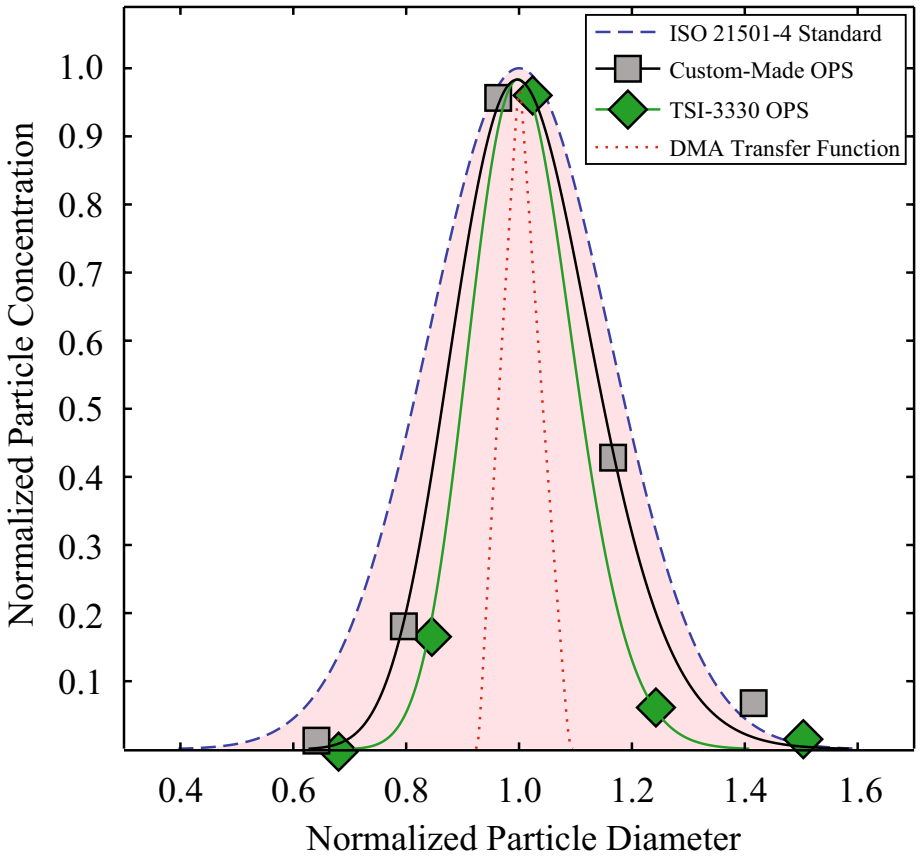

Fig. 7. Comparison of the sizing resolution of the custom-made OPS-OS with that of the TSI-3330 OPS, including limits according to the ISO 21501-4 sizing resolution standards and the resolution of the DMA.

Data availability

Apart from the data of Fig. 2a, all the data presented in the figures of the manuscript are provided in an excel file as a supplement. The data for Fig. 2a are a *.dat file that is almost 1 GB, and considering that this figure is only for illustration purposes, the data can be provided upon request by contacting George Biskos (g.biskos@cyi.ac.cy; g.biskos@tudelft.nl).

Received: 16 August 2024; Accepted: 14 July 2025
Published online: 09 October 2025

References

1. Xu, R. Optical particle counting. In Particle Characterization: Light Scattering Methods, 182–222, Springer, Netherlands (2002).
2. McMurry, P. H. A review of atmospheric aerosol measurements. *Atmos. Environ.* **34**, 1959–1999 (2000).
3. Gozzi, F., Marcelli, A. & Lucci, F. Current status of particulate matter pollution in Europe and future perspectives: A review. *Environ. Sci.* **8**, 1901–1909 (2017).
4. Kim, J. et al. Assessing optical properties and refractive index of combustion aerosol particles through combined experimental and modeling studies. *Aerosol Sci. Technol.* **49**, 340–350 (2015).
5. Lee, S. Y., Chang, H., Ogi, T., Iskandar, F. & Okuyama, K. Measuring the effective density, porosity, and refractive index of carbonaceous particles by tandem aerosol techniques. *Carbon* **49**, 2163–2172 (2011).
6. Ryan, R. T., Blau, H. H., von Thüna, P. C., Cohen, M. L. & Roberts, G. D. Cloud microstructure as determined by an optical cloud particle spectrometer. *J. Appl. Meteorol. Climatol.* **11**, 149–156 (1972).
7. Renard, J.-B. et al. LOAC: a small aerosol optical counter/sizer for ground-based and balloon measurements of the size distribution and nature of atmospheric particles – Part 1: Principle of measurements and instrument evaluation. *Atmos. Meas. Tech.* **9**, 1721–1742 (2016).
8. Garimella, S., Huang, Y.-W., Seewald, J. S. & Cziczo, D. J. Cloud condensation nucleus activity comparison of dry- and wet-generated mineral dust aerosol: the significance of soluble material. *Atmos. Chem. Phys.* **14**, 6003–6019 (2014).
9. Szymanski, W. W., Nagy, A. & Czitrovszky, A. Optical particle spectrometry—Problems and prospects. *J. Quant. Spectrosc. Radiat. Transf.* **110**, 918–929 (2009).
10. Rosati, B. et al. The white-light humidified optical particle spectrometer (WHOPS)—a novel airborne system to characterize aerosol hygroscopicity. *Atmos. Meas. Tech.* **8**, 921–939 (2015).
11. Crilley, L. R. et al. Evaluation of a low-cost optical particle counter (Alphasense OPC-N2) for ambient air monitoring. *Atmos. Meas. Tech.* **11**, 709–720 (2018).
12. Bezantakos, S., Schmidt-Ott, F. & Biskos, G. Performance evaluation of the cost-effective and lightweight Alphasense optical particle counter for use onboard unmanned aerial vehicles. *Aerosol Sci. Technol.* **52**, 385–392 (2018).
13. Mei, F. et al. Performance assessment of portable optical particle spectrometer (POPS). *Sensors* **20**, 6294 (2020).

14. Smith, H. R. et al. The Universal Cloud and Aerosol Sounding System (UCASS): a low-cost miniature optical particle counter for use in dropsonde or balloon-borne sounding systems. *Atmos. Meas. Tech.* **12**, 6579–6599 (2019).
15. Hill, M. *et al.* A Compact lightweight aerosol spectrometer probe (CLASP). *J. Atmos. Ocean Technol* .**25**, (2008).
16. Hermann, M. et al. An optical particle size spectrometer for aircraft-borne measurements in IAGOS-CARIBIC. *Atmos. Meas. Tech.* **9**, 2179–2194 (2016).
17. Gao, R. S. et al. A light-weight, high-sensitivity particle spectrometer for PM2.5 aerosol measurements. *Aerosol Sci. Technol.* **50**, 88–99 (2016).
18. Kasparoglu, S., Islam, M. M., Meskhidze, N. & Petters, M. D. Characterization of a modified printed optical particle spectrometer for high-frequency and high-precision laboratory and field measurements. *Atmos. Meas. Tech.* **15**, 5007–5018 (2022).
19. Sousan, S., Regmi, S. & Park, Y. M. Laboratory evaluation of low-cost optical particle counters for environmental and occupational exposures. *Sensors* **21**, 4146 (2021).
20. ISO/DIS 21501-1 Determination of particle size distribution — Single particle light interaction methods Part 1: Light scattering aerosol spectrometer, available at: https://www.iso.org/standard/81877.html
21. ISO 21501-4:2018 Determination of particle size distribution — Single particle light interaction methods Part 4: Light scattering airborne particle counter for clean spaces, available at: https://www.iso.org/standard/58073.html
22. Berisha, S., van Dijk, T., Bhargava, R., Carney, P. S. & Mayerich, D. BIM-Sim: Interactive simulation of broadband imaging using Mie theory. *Front. Phys.* **5**, (2017).
23. Hahn, D. Light Scattering Theory. (2004).
24. Lockwood, D. J. Rayleigh and Mie scattering. In Encyclopedia of Color Science and Technology (ed. Luo, M. R.) 1097–1107, Springer (2016).
25. Rosenberg, P. et al. Particle sizing calibration with refractive index correction for light scattering optical particle counters and impacts upon PCASP and CDP data collected during the Fennec campaign. *Atmos. Meas. Tech.* **5**, 1147–1163 (2012).
26. Chen, B. T., Cheng, Y. S. & Yeh, H. C. Experimental responses of two optical particle counters. *J. Aerosol Sci.* **15**, 457–464 (1984).
27. Liu, B. Y. H., Berglund, R. N. & Agarwal, J. K. Experimental studies of optical particle counters. *Atmos. Environ.* **1967**(8), 717–732 (1974).
28. Okokpujie, I. P., Bolu, C. A., Ohunakin, O. S., Akinlabi, E. T. & Adelekan, D. S. A review of recent application of machining techniques, based on the phenomena of CNC machining operations. *Procedia Manuf.* **35**, 1054–1060 (2019).
29. Mukhtarkhanov, M., Perveen, A. & Talamona, D. Application of stereolithography based 3D printing technology in investment casting. *Micromachines* **11**, 946 (2020).
30. Maines, E. M., Porwal, M. K., Ellison, C. J. & Reineke, T. M. Sustainable advances in SLA/DLP 3D printing materials and processes. *Green Chem.* **23**, 6863–6897 (2021).
31. NIST Traceable Size Standards, available at: https://magsphere.com/store/NIST.html
32. Locci-Lopez, D., Zhang, R., Oyem, A. & Castagna, J. The Multi-Scale Fourier Transform, SEG International Exposition and 88th Annual Meeting, 4176-4180 (2018).
33. TSI_CC-117_The_Purpose_and_Application_of_ISO_21501-4_AppNote.pdf.
34. LabVIEW Programming Reference Manual, Peak Detector VI, available at: https://www.ni.com/docs/en-US/bundle/labview-api-ref/page/vi-lib/analysis/8numeric-llb/peak-detector-vi.html?srsltid=AfmBOoq75SGn8N1ozfYpHEgqfD186IZgbL5LQl_EFOAsn0SkupDMDDvS
35. The k-ω Turbulence Model, available at: https://doc.comsol.com/5.5/doc/com.comsol.help.cfd/cfd_ug_fluidflow_single.06.090.html.
36. Hassan, H., Guo, T. & Vlachos, P. *Flow Field Evolution and Entrainment in a Free Surface Plunging Jet*. (2019).
37. Vasilatou, K. et al. Calibration of optical particle size spectrometers against a primary standard: Counting efficiency profile of the TSI Model 3330 OPS and Grimm 11-D monitor in the particle size range from 300 nm to 10 μm. *J. Aerosol Sci.* **157**, 105818 (2021).
38. Vasilatou, K. et al. Extending traceability in airborne particle size distribution measurements beyond 10 μm: Counting efficiency and unit-to-unit variability of four aerodynamic particle size spectrometers. *Aerosol Sci. Technol.* **57**, 24–34 (2022).

Acknowledgements

This work has received funding from the EMME-CARE project, which is funded by the European Union's Horizon 2020 research and innovation programme under grant agreement No. 856612 and the Cyprus Government.

Author contributions

CL and GB conceived the experiments, CL, CS, SB and NH designed and built the OPS prototype, CL conducted the experiments and analyzed the results. CL and GB wrote the original draft and all authors reviewed the manuscript.

Declarations

Competing interests

The authors declare no competing interests.

Additional information

Supplementary Information The online version contains supplementary material available at https://doi.org/10.1038/s41598-025-11785-2.

Correspondence and requests for materials should be addressed to G.B.

Reprints and permissions information is available at www.nature.com/reprints.

Publisher's note Springer Nature remains neutral with regard to jurisdictional claims in published maps and institutional affiliations.

Open Access This article is licensed under a Creative Commons Attribution-NonCommercial-NoDerivatives 4.0 International License, which permits any non-commercial use, sharing, distribution and reproduction in any medium or format, as long as you give appropriate credit to the original author(s) and the source, provide a link to the Creative Commons licence, and indicate if you modified the licensed material. You do not have permission under this licence to share adapted material derived from this article or parts of it. The images or other third party material in this article are included in the article's Creative Commons licence, unless indicated otherwise in a credit line to the material. If material is not included in the article's Creative Commons licence and your intended use is not permitted by statutory regulation or exceeds the permitted use, you will need to obtain permission directly from the copyright holder. To view a copy of this licence, visit http://creativecommons.org/licenses/by-nc-nd/4.0/.

© The Author(s) 2025